GEOPHYSICS, VOL. 88, NO. 5 (SEPTEMBER-OCTOBER 2023); P. WB45–WB54, 11 FIGS.
10.1190/GEO2022-0521.1

Cooperative joint inversion of magnetotelluric and microseismic data for imaging The Geysers geothermal field, California, USA

Evan Schankee Um[1], Michael Commer[1], Roland Gritto[2], Jared R. Peacock[3], David L. Alumbaugh[1], Steve P. Jarpe[4], and Craig Hartline[5]

ABSTRACT

The Geysers geothermal field located in northern California, USA, is the world's largest electricity-generating geothermal facility. To delineate the spatio-temporal distribution of reservoir steam and recharge water, we have collected microseismic and magnetotelluric (MT) data using a dense array of stations in 2021. The microseismic and MT data have been inverted together using a 3D cooperative joint inversion workflow. The joint inversion exploits a cross-gradient structural constraint because electrical conductivity structures observed in the geothermal field are strongly correlated with V_P/V_S structures. To mitigate convergence issues associated with 3D large-scale joint inversion, the scheme is split into small manageable inversion subsets. By systematically performing the three inversion subsets and exchanging the structural information between velocity and conductivity models, the cooperative joint inversion mimics the full joint inversion. The 3D joint inversion results agree well with previous 3D microseismic and MT inversion studies. We find that the cooperative joint inversion improves overall MT images in terms of resolution and consistency with respect to the V_P/V_S model. The joint inversion also further reduces the MT data misfit. In contrast, the joint inversion does not significantly improve microseismic images because MT inversion produces low-resolution conductivity images with respect to microseismic images in depth of investigation (i.e., 1–5 km) and thus does not provide sufficient structural details that are required for improving microseismic images.

INTRODUCTION

Geothermal resources are an important renewable energy source found in the western United States and many other areas around the world (Blackwell et al., 2006; Tester et al., 2006; Breede et al., 2013; Kana et al., 2015; Lu, 2018). The development of geothermal resources is conceptually simple. Deep wells are drilled into permeable hydrothermal reservoirs. Hot water and steam are pumped to the earth's surface for generating electricity in geothermal power plants and heating buildings and other structures through direct use applications. Compared with other renewable energy sources, such as wind and solar power, geothermal power plants continuously produce electricity and have served as a baseload energy resource (Dobson et al., 2020).

Efficiently developing and operating geothermal reservoir fields requires monitoring and characterizing microseismic activities and the distribution of geothermal fluids and steam inside and around hydrothermal reservoirs. Geophysical methods play an important role in monitoring and characterization. For example, microseismic inversion can not only be used to determine the locations of microseismic events associated with hydraulic fractures but also can delineate P- and S-wave velocity structures (Wohlenberg and Keppler, 1987; Zhang and Thurber, 2003; Dyer et al., 2008; Oye et al., 2012; Lellouch et al., 2020). The ratio of V_P to V_S can be used for mapping fluids and steam-saturated areas in a geothermal field (Moos and Zoback, 1983; Boitnott and Kirkpatrick, 1997; Gritto and Jarpe, 2014; Lin and Wu, 2018; Gritto et al., 2022).

Manuscript received by the Editor 18 August 2022; revised manuscript received 16 March 2023; published ahead of production 20 April 2023; published online 21 June 2023.
[1]Lawrence Berkeley National Laboratory, Earth and Environmental Sciences Area, Berkeley, California, USA. E-mail: esum@lbl.gov (corresponding author); mcommer@lbl.gov; dalumbaugh@lbl.gov.
[2]Array Information Technology, Berkeley, California, USA. E-mail: roland.gritto@arrayinfotech.com.
[3]U.S. Geological Survey, Menlo Park, California, USA. E-mail: jpeacock@usgs.gov.
[4]Jarpe Data Solutions Inc., Prescott Valley, Arizona, USA. E-mail: sjarpe@gmail.com.
[5]Calpine Corporation, Middletown, California, USA. E-mail: craig.hartline@calpine.com.

Electromagnetic (EM) methods also are useful for monitoring the fluid distribution in a geothermal field because EM is sensitive to electrical conductivity contrasts between conductive water-saturated areas and resistive impermeable host rock or steam-filled areas. Borehole-based EM methods have been used for imaging fluid flow near and around wells (Wilt et al., 2002; Börner et al., 2015; Cuevas, 2019; Castillo-Reyes et al., 2021). The magnetotelluric (MT) method has been a primary EM tool for locating potential geothermal reservoirs and also has been recently applied for monitoring fluid flow in geothermal fields (Wannamaker et al., 2004; Newman et al., 2008; Peacock et al., 2012, 2013, 2020; Munoz, 2014; Lindsey et al., 2016).

Microseismic and MT applications have their own uncertainties and limitations. For example, microseismic inversion depends on the starting velocity model, which is not exactly known a priori, leaving uncertainties in the resulting models (Maxwell et al., 2010). Different microseismic data processing methods applied to the same data set also can result in different interpretations (Hayles et al., 2011). Geothermal sites are inherently noisy due to the continuous operations of pumps, pipelines, and power plants, which complicate the processing of seismic waveform data (Johnston and Shrallow, 2011). Locations of microseismic events do not necessarily indicate currently active and open fluid pathways (Peacock et al., 2012; Hoversten et al., 2015).

In general, MT data can effectively delineate electrically conductive structures on a large scale but are mostly insensitive to thin resistive structures, which can be associated with dry steam regions. As a passive geophysical method, MT also is vulnerable to environmental noise due to powerlines commonly found at geothermal electric-energy generating facilities (Bedrosian et al., 2003; Newman et al., 2008; Peacock et al., 2012, 2020). Because high-frequency EM waves attenuate more rapidly within the earth, the resolution of MT decreases with increasing depth of investigation (Chave and Jones, 2012), leaving uncertainties in interpreting deep geothermal structures in detail.

In this case study, we concurrently acquire microseismic and MT data using arrays of seismic and MT instruments at The Geysers geothermal field located in northern California. We invert the microseismic and MT data together using a 3D cooperative joint inversion method (Um et al., 2014). This cooperative joint inversion workflow was originally developed for inverting large-scale marine seismic and controlled-source EM (CSEM) data together for subsalt imaging. In this paper, we test the workflow using real microseismic and MT data acquired at The Geysers geothermal field and examine if the joint inversion can improve the overall resolution and consistency of the geophysical models to more accurately characterize the distribution of geothermal fluid and steam. Our paper is organized as follows. First, we briefly introduce the 3D cooperative joint inversion workflow used in this study. Second, we describe microseismic and MT data acquisition at The Geysers. Third, we perform 3D standalone microseismic and MT inversion, compare the standalone inversion models to 3D joint inversion models, and evaluate the values of the joint microseismic-MT inversion for monitoring geothermal fluid.

COOPERATIVE JOINT INVERSION FOR MICROSEISMIC AND MT DATA

The joint inversion aims to find a set of more consistent earth property models (e.g., velocity and conductivity) by simultaneously fitting multiple sets of geophysical data to the models. Commonly used joint inversions can be grouped into two approaches. One approach uses petrophysical relationships to link multiple geophysical attributes (e.g., Harris and MacGregor, 2006; Hoversten et al., 2006). The other approach is based on the structural similarity among different geophysical property models (Haber and Oldenburg, 1997; Gallardo and Meju, 2003; Gallardo and Meju, 2007). The joint inversion approach used in this work uses the latter, i.e., structural similarity. In this study, the structural similarity is achieved in the course of inversion by adding a cross-gradient (CG) constraint term to an objective function as outlined by Gallardo and Meju (2003). The role of this CG term can be explained as follows. If the spatial gradients of structures in two geophysical models are aligned in parallel, then the CG term becomes zero. If a nonvanishing CG term (i.e., a nonzero angle between the two spatial gradient vectors) exists at a given position, structures in these models are forced to change to minimize the CG term. If the gradient vector vanishes in one model, the term reduces to zero, allowing independent boundaries to exist in the other model.

The CG-based joint inversion is well suited to imaging geothermal fluids and steam at The Geysers because seismic velocity and electrical conductivity models are expected to have structural similarities. For example, at The Geysers, areas of high fluid saturation typically correlate with a high ratio of V_P to V_S (Boitnott and Kirkpatrick, 1997; Gritto et al., 2013, 2022) and are likely more conductive than steam-filled areas. Similarly, low V_P/V_S ratios are typically observed in dry steam-dominated areas. Such areas show relatively low electrical conductivity values. Accordingly, using the CG constraint, the joint inversion can find a set of velocity and conductivity models that are consistent with each other.

In general, the objective function ($\varnothing$) for the joint seismic-MT inversion with the CG constraint can be written as

$$\begin{aligned}\varnothing &= \alpha\phi_{\text{data}}^{\text{MT}} + \beta\phi_{\text{data}}^{\text{seismic}} + \lambda_{\text{MT}}\phi_{\text{model}}^{\text{conductivity}} \\ &\quad + \lambda_{\text{seismic}}\phi_{\text{model}}^{\text{velocity}} + \lambda_{cg}\phi_{cg} \\ &= \alpha(D^{\text{MT}}(d_{\text{obs}}^{\text{MT}} - d_{\text{pre}}^{\text{MT}}))^T(D^{\text{MT}}(d_{\text{obs}}^{\text{MT}} - d_{\text{pre}}^{\text{MT}})) \\ &\quad + \beta(D^{\text{seismic}}(d_{\text{obs}}^{\text{seismic}} - d_{\text{pre}}^{\text{seismic}}))^T(D^{\text{seismic}}(d_{\text{obs}}^{\text{seismic}} - d_{\text{pre}}^{\text{seismic}})) \\ &\quad + \lambda_{\text{MT}}(Wm^{\text{conductivity}})^T(Wm^{\text{conductivity}}) \\ &\quad + \lambda_{\text{seismic}}(Wm^{\text{velocity}})^T(Wm^{\text{velocity}}) \\ &\quad + \lambda_{cg}(\nabla m^{\text{velocity}} \times \nabla m^{\text{conductivity}})^T(\nabla m^{\text{velocity}} \times \nabla m^{\text{conductivity}}),\end{aligned} \tag{1}$$

where α, β, λ_{MT}, λ_{seismic}, and λ_{cg} are trade-off parameters that adjust the influence of each term in equation 1; D^{MT} and D^{seismic} are MT and seismic data weighting matrices, respectively; $\mathbf{d}_{\text{obs}}$ and $\mathbf{d}_{\text{pre}}$ are vectors of observed data and predicted data, respectively; W is a regularization matrix that approximates the Laplacian operator; $\mathbf{m}^{\text{conductivity}}$ and $\mathbf{m}^{\text{velocity}}$ are vectors of electrical conductivity and velocity model, respectively; and superscript T represents the transpose operator.

Compared to standalone 3D MT or seismic inversion that includes only one data and one regularization term, equation 1 includes multiple data and regularization terms along with the CG constraint term. As more terms are added to the objective function, the 3D joint inversion becomes increasingly nonlinear and often converges to a local minimum (Um et al., 2014). Therefore, a

successful inversion often relies on multiple inversion runs in a trial-and-error fashion. The trade-off parameters inside the objective function also should be carefully chosen and tested to determine their impact on inversion outcomes (Mackie et al., 2007; Commer and Newman, 2008). In general, it is a challenging task to choose a proper set of the six trade-off parameters. Furthermore, joint inversion often requires integrating two or more standalone 3D inversion modules into one. If the modules are based on different data structures or written in different computer languages, it can be time-consuming to integrate them into one joint inversion algorithm.

To mitigate the difficulties associated with the 3D joint inversion, we use a cooperative joint inversion scheme proposed by Um et al. (2014). First, we split equation 1 into three parts as follows:

$$\varnothing^{\mathrm{MT}} = \phi_{\mathrm{data}}^{\mathrm{MT}} + \lambda_{\mathrm{MT}}\phi_{\mathrm{model}}^{\mathrm{conductivity}}, \tag{2}$$

$$\varnothing^{\mathrm{seismic}} = \phi_{\mathrm{data}}^{\mathrm{seismic}} + \lambda_{\mathrm{seismic}}\phi_{\mathrm{model}}^{\mathrm{velocity}}, \tag{3}$$

$$\varnothing^{cg} = (\nabla m^{\mathrm{velocity}} \times \nabla m^{\mathrm{conductivity}})^{T}(\nabla m^{\mathrm{velocity}} \times \nabla m^{\mathrm{conductivity}}). \tag{4}$$

Equations 2–4 represent an objective function for MT, seismic data, and CG inversion, respectively. Note that equations 2 and 3 are only a standard objective function for standalone 3D MT and seismic inversion. In other words, we use existing MT and microseismic inversion tools in this cooperative joint inversion without any modification. We use the modular system for electromagnetics (ModEM) (Kelbert et al., 2014) for the MT inversion and finite-difference double-distance tomography (tomoFDD) (Zhang and Thurber, 2006; Gritto et al., 2013) for the microseismic inversion.

Equation 4 provides a structural link between 3D velocity and conductivity models. Equation 4 is minimized using the nonlinear conjugate gradient method with a line-search algorithm (Newman and Hoversten, 2000; Commer and Newman, 2008). During the minimization, one model is fixed as a reference and the other model is free to change. Note that equation 4 does not include the data part. Therefore, minimizing equation 4 does not require solving computationally expensive forward modeling. By splitting equation 1 into equations 2–4, we reduce the nonlinearity of the three objective functions. Thus, the inversion becomes more robust and avoids converging to a local minimum (Um et al., 2014). For more detail, the reader is referred to the papers cited here.

By minimizing equations 2–4 and exchanging the structural information between the 3D velocity and conductivity models as shown in Figure 1, the cooperative joint inversion mimics the full joint inversion as described next. First, standalone 3D microseismic and MT inversions are completed. Microseismic and MT inversion resolution can vary, depending on sensor spacing and distribution, and data quantity and quality. Due to the differences in the physics of the two imaging techniques, MT inversion can image much deeper than microseismic inversion as long as quality low-frequency MT data can be collected. The high-frequency MT data can have high resolution in the near surface. However, from 1 km to 5 km in depth at The Geysers where the number of earthquakes occurred is highest, microseismic inversion coupled with the high spatial sensor coverage produces higher resolution for imaging the geothermal reservoir than MT inversion (Gritto et al., 2022; Peacock et al., 2022).

Accordingly, it is reasonable to first infuse structural information from the microseismic inversion model to the MT inversion model. This is realized through the CG inversion (i.e., minimizing equation 4) in which the velocity model (i.e., V_P/V_S) is fixed as a reference model and the conductivity model is free to change. The resulting conductivity model resembles the V_P/V_S model but likely shows a large data misfit because the CG inversion does not include the data portion. To reduce the data misfit, the resulting conductivity model is used as a new starting model for a subsequent standalone MT inversion. We call this step the refinement process. The role of the refinement process is to precondition an MT starting model with structural information from the microseismic inversion model. The refinement process and subsequent MT inversion are stopped when the MT data misfit no longer decreases.

Next, we infuse the structural information from the refined conductivity model to the velocity model. Again, we perform the CG inversion in which the conductivity model is fixed as a reference model and the velocity model is free to change. More specifically, the V_S model is free to change, but the V_P model is fixed because V_P/V_S is inversely correlated with V_S, but not correlated with V_P

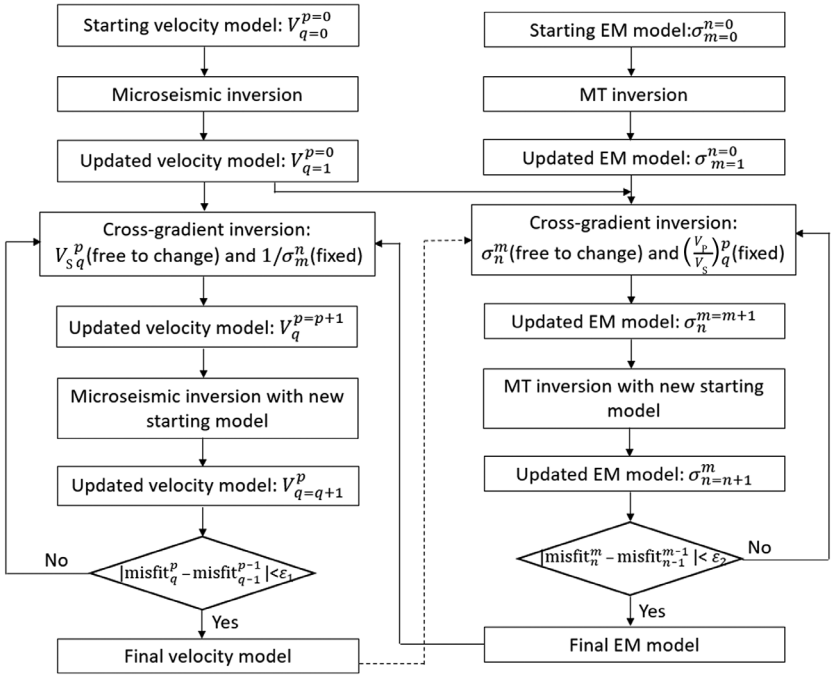

Figure 1. The cooperative joint inversion workflow (Um et al., 2014). Minimization of equations 2–4 represents the MT inversion, the microseismic inversion, and the CG inversion, respectively. Here, V and σ are seismic and conductivity models, respectively. Their superscript and subscript represent the number of CG inversion and standalone inversion performed during the cooperative inversion process.

(Gritto et al., 2013). The resulting velocity model is used as a new starting model for the subsequent 3D microseismic inversion. The refinement process continues until the microseismic data misfit no longer decreases. This completes one full refinement cycle. When necessary, one can start another full refinement cycle (the broken line in Figure 1) by using the final velocity model for refining the conductivity model.

MICROSEISMIC AND MT DATA ACQUISITION AT THE GEYSERS GEOTHERMAL FIELD

The Geysers geothermal field (Figure 2) is located approximately 70 miles north of San Francisco, California, and is currently the largest producing geothermal field in the world (Goyal and Conant, 2010; Dobson et al., 2020). It reached peak production in 1987. Since this time, the steam production has been in gradual decline (Dobson et al., 2020). To increase the production and extend the life of the geothermal resource, wastewater from nearby communities has been treated and injected into the reservoir (Sanyal and Enedy, 2011). Since the injection program started, the number of small earthquakes ranging from magnitudes 0.5 and 2.0 has substantially increased, enabling us to use microseismic techniques to image velocity structures and infer the distribution of geothermal fluid in the area.

In 2018, the 48-station permanent Berkeley Geysers (BG) seismic network was supplemented by the 92-station temporary California Energy Commission (CEC) seismic network. Although the stations of the BG network are distributed throughout and beyond the active steam reservoir, the 92 stations of the CEC network were densely deployed in the northwest Geysers to support the development of geothermal operations with an average interstation distance of 500 m distributed over a 5 km × 5 km area. Figure 3 shows the locations of the two seismic networks within the reservoir boundaries denoted by the red polygon, whereas surface traces of the known faults are indicated by black lines. The locations of the 92 temporary CEC-network stations and of the 48 permanent BG-network stations are shown, respectively, by the red and green triangles. The permanently deployed BG network has been in operation for several decades and has been expanded and upgraded multiple times. At present, it comprises 48 surface and shallow borehole stations with 4.5 Hz and 2 Hz 3C sensors. Data from the BG stations are telemetered to a local computer at a local facility, where the seismic data are preprocessed for event detection and waveforms are formatted. The data are subsequently transmitted to a processing center for further analysis. The CEC stations are comprised of 4.5 Hz 3C geophones. The seismic data are recorded locally on SD cards and collected on a quarterly basis.

Combining seismic data from the two networks improves the spatial coverage of the network and the resolution of the tomographic inversions. Processing of the combined seismic network data is conducted to determine P- and S-wave phase arrival times for tomographic seismic imaging of the reservoir heterogeneity. Seismic data processing was based on the software packages PhaseNet (Zhu and Beroza, 2019), a deep-neural-network-based seismic arrival-time picking method. PhaseNet uses 3C seismic waveform data as input and generates probability distributions of P and S arrivals as output, based on thousands of analyst picks of California earthquake network data. The maxima in the probability distributions provide accurate arrival times for P and S waves. The picks of the seismic phase arrivals were weighted by the square of the probability resulting from data processing with PhaseNet and used as D^{seismic} inside $\phi_{\text{data}}^{\text{seismic}}$ in equation 3. This processing step is followed by event association and the location provided by Gamma (Zhu et al., 2022), an algorithm that uses an earthquake phase association based on a Bayesian Gaussian mixture model. The final seismic data set for the microseismic

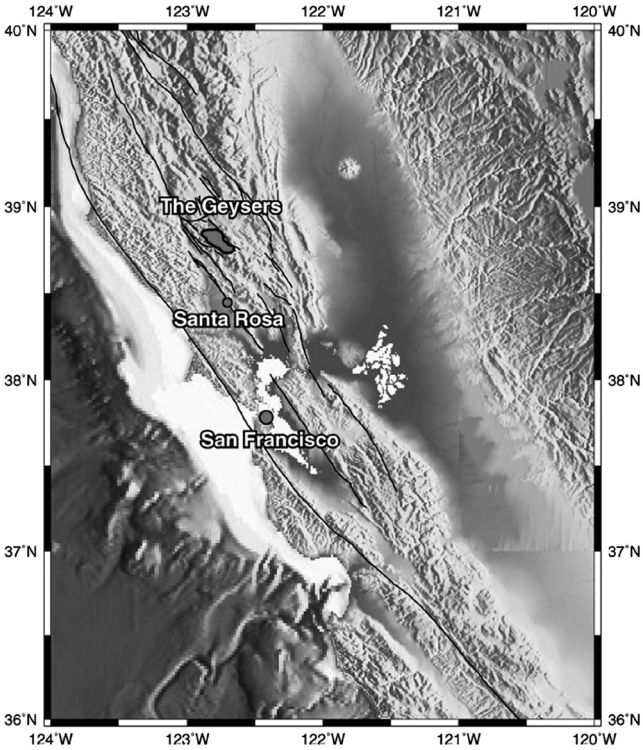

Figure 2. Map of Northern California with the location of The Geysers geothermal field and nearby major cities (from Gritto and Jarpe, 2014). The black lines indicate the surface traces of major faults.

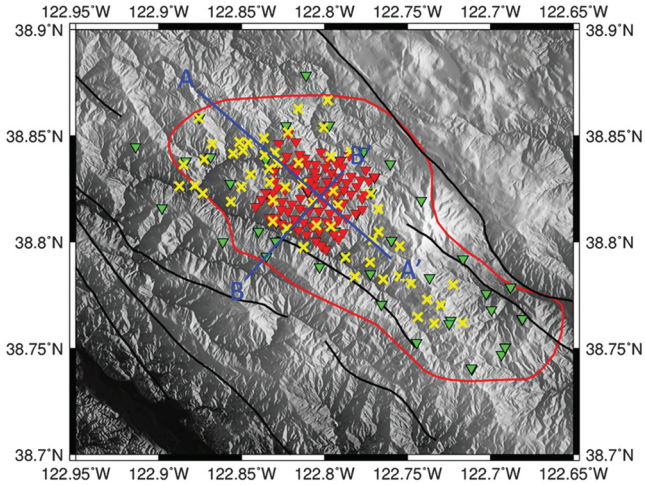

Figure 3. Map (adapted from Gritto et al., 2022) showing the permanent seismic network (green triangles), the temporary seismic network (red triangles), and MT stations (yellow crosses) at The Geysers geothermal reservoir. The outline of the reservoir steam field is given by the red polygon and the surface traces of the known faults are indicated by the black lines. Profiles A-A′ and B-B′ denote the locations of the cross-sectional views shown in Figures 6–10.

inversion consists of 45,904 events recorded between June 2018 and February 2021.

The 41 MT stations used in the 2017 MT campaign (Peacock et al., 2020, 2022) were repeated along with an additional 14 MT stations in the southern part of The Geysers field, as shown in Figure 3. The 2021 MT data were collected in a period range of 0.002 s and 2000 s with the same data loggers, magnetic coil receivers, and electric dipole receivers where possible. Each MT station included two horizontal orthogonal ANT-4 magnetic induction coils and two orthogonal electrical dipoles with a nominal length of 50 m, dependent on vegetation and topography. Ag-AgCl Stelth 1 Borin electrodes were placed in a saturated canvas bag of bentonite clay to reduce the contact resistance. Each channel was connected to a five-channel 32-bit Zonge International ZEN data logger. The data were recorded on a repeating schedule of 10 min sampling at 4096 samples/second and 5 h and 50 min sampling at 256 samples/second. The schedules were set such that all recording instruments recorded the sampling rates synchronously to allow for remote reference processing. MT transfer functions were estimated using a robust remote reference bounded-influence processing code, BIRRP (Chave and Thomson, 2004). Coherency sorting, downweighting of leverage points, and multiple remote references will reduce the influence of cultural noise. The MT data can be weighted with error floors of 5% of the maximum eigenvalue of the impedance tensor, the same weight for all tensor components (Peacock et al., 2022). The weights are used as D^{MT} inside $\phi^{\mathrm{MT}}_{\mathrm{data}}$ in equation 2. These processes are critically important in an electromagnetically noisy environment, such as The Geysers geothermal field.

A comparison of MT responses between 2017 and 2021 data shows that measurements are essentially repeated (Figure 4). A few new 2021 stations show new noise sources and some other stations with improved data quality compared with the 2017 data. Note that the 3D MT inversion for the 2017 data is used later as a starting model for inverting the newly acquired 2021 MT data. Because the seasonal near-surface distortions (e.g., soil moisture) can result in a static shift in the apparent resistivity, and we are mainly interested in deep geothermal structures, we matched the apparent resistivity of the first two decades of the 2021 data with the 2017 data (Peacock et al., 2020). Overall, Figure 4 shows an increase in apparent electrical resistivity between 2017 and 2021 MT campaigns.

3D STANDALONE INVERSION FOR MICROSEISMIC AND MT DATA

Before we evaluate the 3D cooperative joint inversion for the microseismic and MT data, we perform standalone inversions of each data type separately (the top two steps of Figure 1) and then compare the imaging results. Microseismic studies and imaging have been extensively performed over the area in the past decades (e.g., Boitnott and Kirkpatrick, 1997; Gritto et al., 2013; Gritto and Jarpe, 2014). Therefore, a 3D starting velocity model for the microseismic inversion is taken from a recent microseismic study (Gritto et al., 2013). The model is mapped onto the microseismic inversion grids that consist of $71 \times 71 \times 27$ grid points with a uniform grid spacing of 305 m in the horizontal and vertical directions. The standalone inversion is performed by minimizing the misfit between recorded and predicted traveltimes. The regularization parameter is set to 5000 by trial and error. Figure 5a shows the misfit history as a function of inversion iterations. The misfit did not change further only after one iteration and the subsequent misfit history of the first standalone inversion was not plotted here. This simple convergence is an indication that the 3D starting model is already close to a good representation of velocity structures in the reservoir.

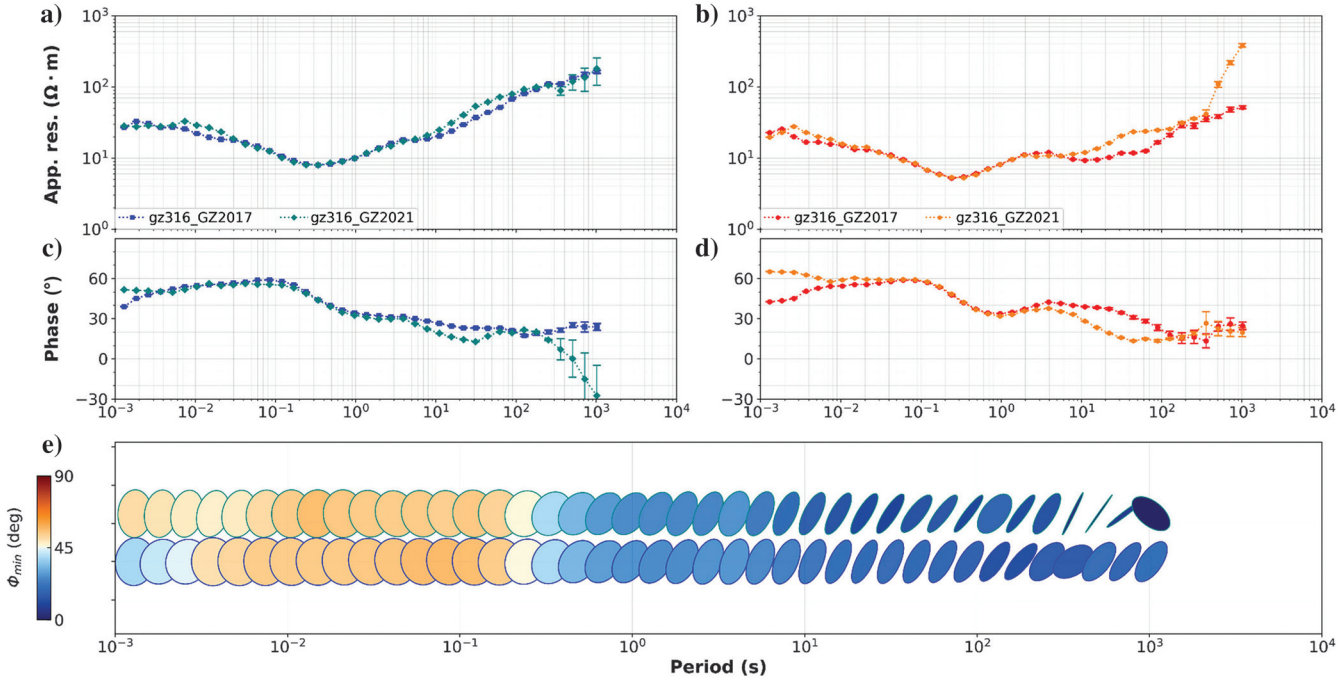

Figure 4. Comparison of MT data from 2017 (blue and red) and 2021 with a static correction to match 2017 data (green and gold). (a and b) The apparent resistivity plots, which are affected by near-surface distortions. This was corrected by matching the first decades of the 2021 data to the 2017 apparent resistivity. (c and d) The impedance phase. (e) Phase tensor representations of the impedance tensor.

In this study, we focus on examining the ratio of V_P to V_S model rather than individual V_P and V_S models because the V_P/V_S model can be used to deduce the spatial distribution of water and steam saturation (Boitnott and Kirkpatrick, 1997; Gritto et al., 2013). High and low V_P/V_S anomalies are correlated with water-saturated and steam-filled areas, respectively. After standalone microseismic and MT inversion, we compare V_P/V_S structures to conductivity structures on two vertical profiles that were extracted from the 3D inversion models. The two profiles were extensively examined in previous research (Gritto et al., 2013, 2022), and thus we also use them here for comparison purposes. Figures 6 and 7 show V_P/V_S and conductivity structures that were extracted along profiles A-A′ and B-B′ from the 3D inversion models, respectively. On profile A-A′ (Figure 6a), the shallow steam reservoir (denoted by the black arrow) is indicated by the orange and red colors (V_P/V_S = 1.4 − 1.6) dipping toward the southeast direction and is connected with larger central steam structures extending beyond 5 km in depth. Profile B-B′ (Figure 7a) shows that the upper steam field is connected to the lower one. Overall, the spatial distribution of V_P/V_S closely agrees with previous microseismic studies and borehole observations (Gritto et al., 2022).

A starting conductivity model for the 3D MT inversion of the data collected in 2021 is taken from an inverted conductivity model from the MT data acquired at The Geysers geothermal field in 2017 (Peacock et al., 2020). The MT inversion grids consist of 70 × 80 × 70 grids points. The central part of the MT model is discretized using 50 and 60 uniform 200 m cells in the x- and y-directions, respectively, with the remaining horizontal cells serving as padding cells. In the vertical direction, uniform 30 m cell spacing is used from the surface to z = 1200 m, and then the cell size gradually increases. The standalone inversion with 2021 MT data converged after 73 iterations, as shown in Figure 5b. The regularization lambda is initially set to 10 and gradually decreases to 10^{-8}. This initial regularization lambda is an order of magnitude smaller than one used in inversion for 2017 MT data (Peacock et al., 2020) because the starting model (i.e., the final inversion model with 2017 MT data) is already fairly smooth. Figure 5b shows changes in the regularization parameter in the course of inversion. The motivation behind choosing the smaller initial lambda is to sharpen a subsequent MT image during the refinement process because The Geyser reservoir field is known to be highly heterogeneous (Gritto et al., 2022).

Figures 6b and 7b show cross-sectional views of the new MT inversion model along the two profiles in Figure 3. The MT inversion result is plotted in terms of electrical conductivity rather than resistivity because the conductivity is positively correlated with V_P/V_S. In general, low electrical conductivity regions indicating steam-filled or dry host rocks are roughly corre-

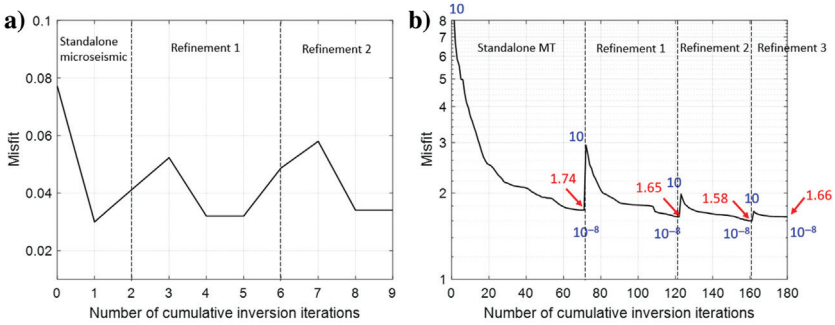

Figure 5. The misfit history plots. (a) The microseismic data misfit history plot. (b) The MT data misfit history plot. The x-axis is the number of cumulative inversion iterations including the first standalone inversion and subsequent refinement inversion processes. The broken vertical lines divide each inversion into segments. For microseismic inversion and subsequent refinement processes, the regularization parameter is set to 5000. For each MT inversion, the regularization parameter (blue) changes from 10 to 10^{-8}. The final misfit after each refinement process is denoted in red.

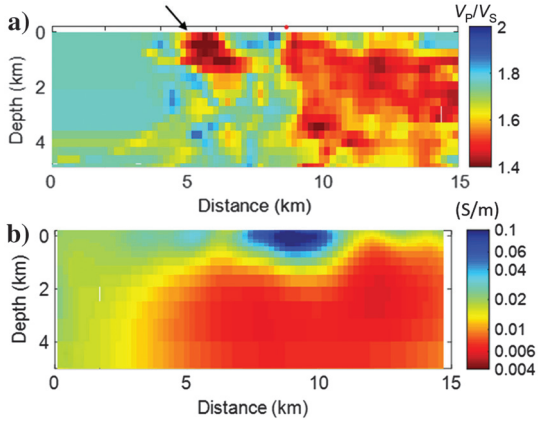

Figure 6. Cross-sectional views of standalone (a) V_P/V_S estimates and (b) MT conductivity estimates along profile A-A′ shown in Figure 3. A is on the left (0 km) and A′ is on the right.

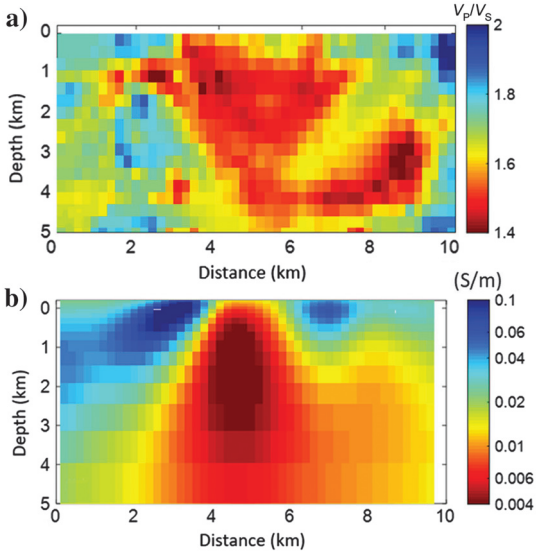

Figure 7. Cross-sectional views of standalone (a) V_P/V_S estimates and (b) MT conductivity estimates (S/m) along profile B-B′ shown in Figure 3. B is on the left (0 km) and B′ is on the right.

lated with low V_P/V_S regions shown in Figures 6a and 7a. Nonetheless, it is difficult to directly map low conductivity regions to low V_P/V_S regions because of the relatively low resolution of the MT images. For example, the shallow steam reservoir (denoted by the black arrow in Figure 6a) would not be confidently identified on profile A-A′ of the conductivity model (Figure 6b) without comparing the model against the corresponding V_P/V_S model (Figure 6a).

COOPERATIVE JOINT INVERSION FOR MICROSEISMIC AND MT DATA

After the standalone microseismic and MT inversions (the first three rows of Figure 1) are completed, we incorporate structural information from one property model into the other. Because the V_P/V_S model (Figures 6a and 7a) shows more structural details than the MT conductivity model (Figures 6b and 7b), we first incorporate the seismic structure into the conductivity model (the remaining right part of Figure 1) using the CG inversion. To perform the CG inversion, the two models need to be on common grids. We choose the microseismic inversion grids as the common grid for convenience because the grid is uniform in all three directions. Thus, the MT inversion model is mapped onto the microseismic inversion grid. During the CG inversion, the V_P/V_S model is fixed as a structural reference whereas the conductivity model is free to change. The CG inversion (equation 4) does not include any forward modeling for reducing the MT data misfit. Rather, its goal is to produce a new starting conductivity model that is close to the structures represented in the V_P/V_S model. In other words, a new starting model is generated without considering the data misfit. As a result, the data misfit history (Figure 5b) shows that, during each step of the refinement process, the initial data misfit is larger than the final misfit of the previous MT inversion. With the new starting model, we then repeat the MT inversion until the refinement process no longer reduces the data misfit. In this example, the third refinement process produces a larger final data misfit (i.e., 1.66) than the second refinement (i.e., 1.58). We therefore choose the second refinement results as the final MT inversion model.

Figures 8 and 9 show the final MT conductivity images along the two profiles. Compared to the standalone MT inversion (Figures 6 and 7), the cooperative joint inversion not only makes the MT images more consistent with the microseismic images but also introduces more detailed structures to the MT images. Now, the shallow low-conductivity steam reservoir (denoted by the black arrow) is clearly identified on profile A-A′ (Figure 8b). Its dipping trend also is consistent with that found in the microseismic image (Figure 6a). On the right side of the profile A-A′ (Figure 8b) and the center of the profile B-B′ (Figure 9b), the deep low-conductivity structures closely resemble V_P/V_S structures found in the same regions of the microseismic inversion (Figures 6a and 7a) in terms of geometry and attribute magnitude.

Although the joint inversion increases the complexity of the conductivity model, the MT data may not be sufficiently sensitive to all these small-scale conductivity structures. For example, some small-scale resistive structures at shallow depths would be more dependent on the CG inversion. They would be mainly introduced by the CG inversion and then remain unchanged in the course of the MT inversion. It would be difficult to precisely determine how well the small-scale structures truly match variations in earth conductivity without additional constraints or evidence. However, the observations that (1) the initial data misfit after each CG inversion is smaller than the previous initial misfit and (2) the final conductivity model from the joint inversion produces a similar/slightly smaller data misfit than the standalone MT inversion provide some evidence that these higher resolution conductivity structures are real.

Examining intermediate models and data in the course of the joint inversion is useful for understanding the role of the joint inversion. During each refinement process, the joint inversion first enforces the structural similarity between the conductivity (free to change) and V_P/V_S (fixed reference) models through the CG inversion. The resulting conductivity model is used as a new starting model for the regular MT inversion without any structural constraints. A comparison of the starting conductivity model with the final model at each refinement process tells us what small-scale structures were introduced by the CG inversion and what other structures were actually recovered/refined by the MT inversion. As shown in Figure 10, the

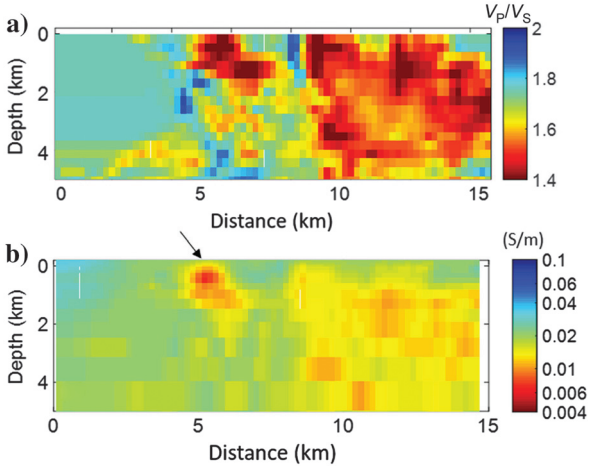

Figure 8. Cross-sectional views of the final cooperative joint inversion results along profile A-A′. (a) The V_P/V_S estimates and (b) the MT conductivity estimates.

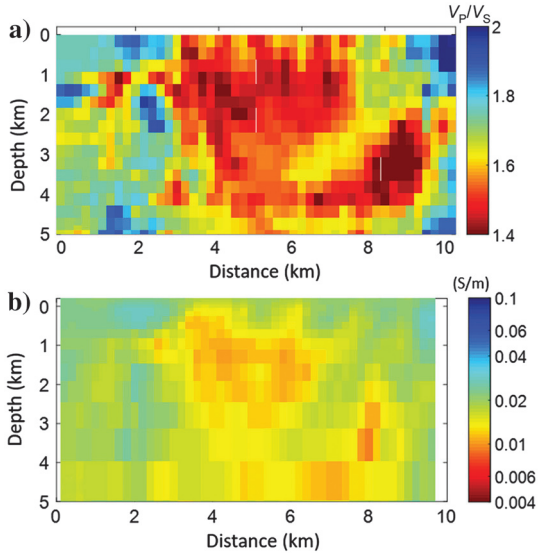

Figure 9. Cross-sectional views of the final cooperative joint inversion results along profile B-B′. (a) The V_P/V_S estimates and (b) the MT conductivity estimates.

shallow resistive structures (denoted by the black broken circle) were more dependent on the CG inversion. In other words, they were mainly imaged during the CG inversion step. In contrast, the deep structures (denoted by the red broken ellipsoid) were mainly refined by the MT inversion. Figure 11 compares the observed MT responses to those from the standalone and final joint inversion conductivity model at MT stations above the shallow and deep resistive structures. Overall, moderate improvements in data misfits are observed, although the joint inversion makes the final conductivity model (Figures 8b and 9b) highly complex compared to the initial MT inversion (Figures 6b and 7b). In short, the joint inversion makes the MT images comparable to the seismic images by incorporating seismic structures into the conductivity model as well as improving the MT inversion.

Next, we examine if the cooperative joint inversion can improve the microseismic inversion by performing the remaining left part of the workflow (Figure 1), which consists of (1) the refinement process in which the final MT image (Figures 8b and 9b) is fixed as a structural reference and the velocity model is free to change and (2) the subsequent standalone microseismic inversion. The misfit history curve for the refinement processes is plotted in Figure 5a. The misfit does not decrease anymore after the first refinement. The V_P/V_S estimates from the final microseismic inversion are shown in Figures 8a and 9a. The cross-sectional views are nearly identical to those from the standalone microseismic inversion images (Figures 6a and 7a). That is, the cooperative joint inversion workflow fails to improve the microseismic inversion. The ineffectiveness of the workflow can be explained by the fact that MT inversion for this particular data acquisition scenario produces lower-resolution conductivity images compared with microseismic images. As a result, the MT images (Figures 8b and 9b) do not contain sufficient structural details to improve the microseismic inversion.

Until now, we have demonstrated that the cooperative joint inversion can produce mutually consistent conductivity and V_P/V_S models. The refinement process in the joint inversion makes MT images delineate deep geothermal structures in detail. However, the enhanced MT images neither improve the V_P/V_S images nor provide new information about deep geothermal structures. Accordingly, in this particular case study, it is natural to ask "what is the value of MT data in this joint inversion analysis?" We think that one important role that the MT data play here is to help us evaluate the overall quality and accuracy of microseismic and MT results. The decrease in MT data misfits adds extra credibility to the microseismic inversion results. The mutual consistency between MT and microseismic images also suggests that MT data were successfully collected in the noisy power-plant environment and were correctly processed and inverted. Before this MT work, it was uncertain if MT acquisition at The Geysers was feasible at all. The higher resolution in the resistivity images, though not providing a significant reduction in data misfits over the nonconstrained images, will provide better estimates of the spatial water saturation in the 3D volume.

More importantly, this study helps us propose an improved EM component for future joint inversion projects with the goal of reducing the resolution mismatch between the EM and microseismic images. There might be a few ways to achieve this goal. For example, one would acquire CSEM data using a limited number of grounded electric dipole sources or consider the z-axis tipper EM (ZTEM) method by which airborne vertical magnetic fields are densely measured and correlated with sparse surface horizontal magnetic fields (Mackie et al., 2007; Commer and Newman, 2008; Alumbaugh et al., 2016; Wannamaker et al., 2017; Velasco et al., 2018). Then, one could invert MT and CSEM/ZTEM data together and examine if the joint inversion of different types of EM data can provide enhanced resolution of conductivity structures.

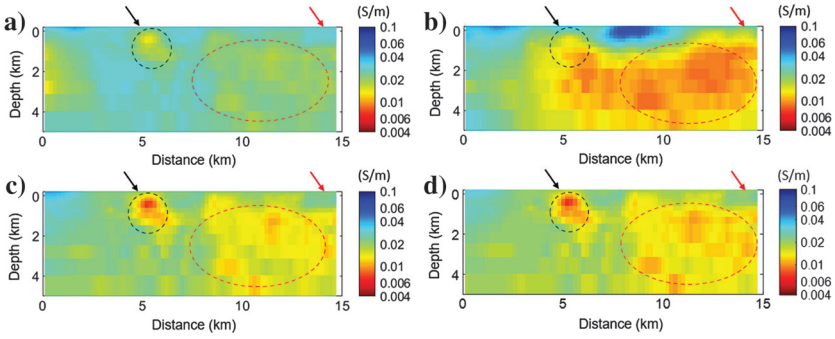

Figure 10. The evolution of electrical conductivity structures (profile A-A′) in the course of the joint inversion. (a and c) A conductivity model only after the CG inversion and (b and d) the subsequent MT inversion model. (a) The conductivity model after the first CG inversion. (b) The conductivity model recovered from the 3D MT inversion using (a) as a starting model. (c) The conductivity model after the second CG inversion. (d) The conductivity model (the final joint-inversion conductivity model) recovered from the 3D MT inversion using (c) as a starting model.

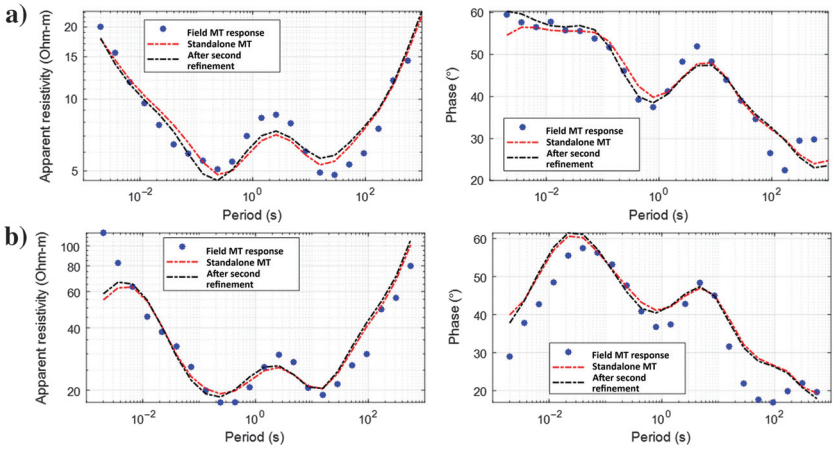

Figure 11. Comparison of the observed and predicted MT responses (Zxy) at (a) an MT station above the shallow resistive structures (Figure 10, denoted by the black arrow) and (b) an MT station above the deep resistive structures (Figure 10, denoted by the red arrow).

CONCLUSION

We collected MT and microseismic data at The Geysers geothermal field in 2021 and inverted the data sets using a cooperative joint inversion workflow. The joint inversion workflow exploits the fact that the electrical conductivity structures within the geothermal field are strongly correlated with V_P/V_S structures. Accordingly, a CG of the conductivity and V_P/V_S models is used as a structural constraint for the joint inversion. We facilitate the joint inversion by splitting the full objective function into three manageable subsets and systematically minimizing each subset.

The fact that the conductivity model from the joint inversion has slightly lower data misfits than the standalone MT inversion provides some evidence that these conductivity structures are real. We were unable to improve deep structures in the microseismic inversion. To improve the seismic imaging part of the joint inversion at The Geysers geothermal field, one needs to reduce the resolution mismatch that exists between conductivity and velocity models by increasing the density of MT stations or supplementing the data set with other types of EM data.

ACKNOWLEDGMENTS

This work was funded by the CEC under contract no. EPC-19-019. We express our gratitude to D. Dreger (UC-Berkeley) and R. Mackie (CGG) for serving as technical advisory committee members. We also thank Calpine for permitting us to collect geophysical data at The Geysers geothermal field, G. Egbert (Oregon State University), and A. Kelbert (U.S. Geological Survey) for making ModEM software available to us. We extend our gratitude to the five GEOPHYSICS reviewers and editor C. Farquharson for providing valuable feedback. M. Mitchell (U.S. Geological Survey) provided an insightful discussion on joint inversion during the internal review process. Any use of trade, firm, or product names is for descriptive purposes only and does not imply endorsement by the U.S. government.

CONFLICTS OF INTEREST

The authors declare no conflicts of interest in preparing this manuscript.

DATA AVAILABILITY

The microseismic and MT data will be made publicly available upon completion of the project in 2023.

REFERENCES

Alumbaugh, D., H. Huang, J. Livermore, and M. Soledad Velasco, 2016, Resistivity imaging in a fold and thrust belt using ZTEM and sparse MT data: First Break, **34**, 65–72, doi: 10.3997/1365-2397.34.4.84071.

Bedrosian, P., U. Weckmann, O. Ritter, C. Hammer, J. Hübert, and A. Jung, 2003, Electromagnetic monitoring of the Groβ Schönebeck stimulation experiment: Kolloquium'Elektromagnetische Tiefenforschung.

Blackwell, D., P. Negraru, and M. Richards, 2006, Assessment of the enhanced geothermal system resource base of the United States: Natural Resources Research, **15**, 283–308, doi: 10.1007/s11053-007-9028-7.

Boitnott, G., and A. Kirkpatrick, 1997, Interpretation of field seismic tomography at The Geysers geothermal field, California: 22nd Workshop on Geothermal Reservoir Engineering, 391–398.

Börner, J. H., M. Bär, and K. Spitzer, 2015, Electromagnetic methods for exploration and monitoring of enhanced geothermal systems — A virtual experiment: Geothermics, **55**, 78–87, doi: 10.1016/j.geothermics.2015.01.011.

Breede, K., K. Dzebisashvili, X. Liu, and G. Falcone, 2013, A systematic review of enhanced (or engineered) geothermal systems: Past, present and future: Geothermal Energy, **1**, 1–27, doi: 10.1186/2195-9706-1-4.

Castillo-Reyes, O., P. Queralt, A. Marcuello, and J. Ledo, 2021, Land CSEM simulations and experimental test using metallic casing in a geothermal exploration context: Valles Basin (NE Spain) case study: IEEE Transactions on Geoscience and Remote Sensing, **60**, 1–13, doi: 10.1109/TGRS.2021.3069042.

Chave, A., and A. Jones, 2012, The magnetotelluric method: Theory and practice: Cambridge University Press.

Chave, A., and D. Thomson, 2004, Bounded influence magnetotelluric response function estimation: Geophysical Journal International, **157**, 988–1006, doi: 10.1111/j.1365-246X.2004.02203.x.

Commer, M., and G. Newman, 2008, Optimal conductivity reconstruction using three-dimensional joint and model-based inversion for controlled-source and magnetotelluric data: 78th Annual International Meeting, SEG, Expanded Abstracts, 609–613, doi: 10.1190/1.3063725.

Cuevas, N., 2019, Surface-borehole electromagnetic method — A review on the technology development and potential for geothermal applications: EAGE/BVG/FKPE Joint Workshop on Borehole Geophysics and Geothermal Energy.

Dobson, P., D. Dwivedi, D. Millstein, N. Krishnaswamy, J. Garcia, and M. Kiran, 2020, Analysis of curtailment at The Geysers geothermal field, California: Geothermics, **87**, 101871, doi: 10.1016/j.geothermics.2020.101871.

Dyer, B., U. Schanz, F. Ladner, M. Haring, and T. Spillman, 2008, Microseismic imaging of a geothermal reservoir stimulation: The Leading Edge, **27**, 856–869, doi: 10.1190/1.2954024.

Gallardo, L., and M. Meju, 2003, Characterization of heterogeneous near-surface materials by joint 2D inversion of DC resistivity and seismic data: Geophysical Research Letters, **30**, 1658, doi: 10.1029/2003GL017370.

Gallardo, L., and M. Meju, 2007, Joint two-dimensional cross-gradient imaging of magnetotelluric and seismic traveltime data for structural and lithological classification: Geophysical Journal International, **169**, 1261–1272, doi: 10.1111/j.1365-246X.2007.03366.x.

Goyal, K., and T. Conant, 2010, Performance history of The Geysers steam field, California, USA: Geothermics, **39**, 321–328, doi: 10.1016/j.geothermics.2010.09.007.

Gritto, R., and S. Jarpe, 2014, Temporal variations of V_P/V_S-ratio at The Geysers geothermal field, USA: Geothermics, **52**, 112–119, doi: 10.1016/j.geothermics.2014.01.012.

Gritto, R., S. Jarpe, and D. Alumbaugh, 2022, New large-scale passive seismic monitoring at The Geysers geothermal reservoir, CA, USA: Proceedings of the 47th Workshop on Geothermal Reservoir Engineering, 1–11.

Gritto, R., S. Yoo, and S. Jarpe, 2013, Three-dimensional seismic tomography at The Geysers geothermal field, CA, USA: Proceedings of the Thirty-Eighth Workshop on Geothermal Reservoir Engineering, 1–12.

Haber, E., and D. Oldenburg, 1997, Joint inversion: A structural approach: Inverse Problems, **13**, 63, doi: 10.1088/0266-5611/13/1/006.

Harris, P., and L. MacGregor, 2006, Determination of reservoir properties from the integration of CSEM, seismic, and well-log data: First Break, **24**, 53–59, doi: 10.3997/1365-2397.24.11.27178.

Hayles, K., R. Horine, S. Checkles, and J. Blangy, 2011, Comparison of microseismic results from the Bakken Formation processed by three different companies: Integration with surface seismic and pumping data: 81st Annual International Meeting, SEG, Expanded Abstracts, 1468–1472, doi: 10.1190/1.3627479.

Hoversten, G., F. Cassassuce, E. Gasperikova, G. Newman, J. Chen, Y. Rubin, Z. Hou, and D. Vasco, 2006, Direct reservoir parameter estimation using joint inversion of marine seismic AVA and CSEM data: Geophysics, **71**, no. 3, C1–C13, doi: 10.1190/1.2194510.

Hoversten, G., M. Commer, E. Haber, and C. Schwarzbach, 2015, Hydrofrac monitoring using ground time-domain electromagnetic: Geophysical Prospecting, **63**, 1508–1526, doi: 10.1111/1365-2478.12300.

Johnston, R., and J. Shrallow, 2011, Ambiguity in microseismic monitoring: 81st Annual International Meeting, SEG, Expanded Abstracts, 1514–1518, doi: 10.1190/1.3627490.

Kana, J., N. Djongyang, D. Raïdandi, P. Nouck, and A. Dadjé, 2015, A review of geophysical methods for geothermal exploration: Renewable and Sustainable Energy Reviews, **44**, 87–95, doi: 10.1016/j.rser.2014.12.026.

Kelbert, A., N. Meqbel, G. Egbert, and K. Tandon, 2014, ModEM: A modular system for inversion of electromagnetic geophysical data: Computers & Geosciences, **66**, 40–53, doi: 10.1016/j.cageo.2014.01.010.

Lellouch, A., N. Lindsey, W. Ellsworth, and B. Biondi, 2020, Comparison between distributed acoustic sensing and geophones: Downhole microseismic monitoring of the FORGE geothermal experiment: Seismological Society of America, **91**, 3256–3268, doi: 10.1785/0220200149.

Lin, G., and B. Wu, 2018, Seismic velocity structure and characteristics of induced seismicity at The Geysers geothermal field, eastern California: Geothermics, **71**, 225–233, doi: 10.1016/j.geothermics.2017.10.003.

Lindsey, N., J. Kaven, N. Davatzes, and G. Newman, 2016, Compartmentalization of the Coso East Flank geothermal field imaged by 3-D

full-tensor MT inversion: Geophysical Journal International, **208**, 652–662, doi: 10.1093/gji/ggw408.
Lu, S., 2018, A global review of enhanced geothermal system (EGS): Renewable and Sustainable Energy Reviews, **81**, 2902–2921, doi: 10.1016/j.rser.2017.06.097.
Mackie, R., M. Watts, and W. Rodi, 2007, Joint 3D inversion of marine CSEM and MT data: 77th Annual International Meeting, SEG, Expanded Abstracts, 574–578, doi: 10.1190/1.3628142.
Maxwell, S., L. Bennett, M. Jones, and J. Walsh, 2010, Anisotropic velocity modeling for microseismic processing: Part 1 — Impact of velocity model uncertainty: 80th Annual International Meeting, SEG, Expanded Abstracts, 2130–2134, doi: 10.1190/1.3513267.
Moos, D., and M. Zoback, 1983, In situ studies of velocity in fractured crystalline rocks: Journal of Geophysical Research: Solid Earth, **88**, 2345–2358, doi: 10.1029/JB088iB03p02345.
Munoz, G., 2014, Exploring for geothermal resources with electromagnetic methods: Surveys in Geophysics, **35**, 101–122, doi: 10.1007/s10712-013-9236-0.
Newman, G., E. Gasperikova, G. Hoversten, and P. Wannamaker, 2008, Three-dimensional magnetotelluric characterization of the Coso geothermal field: Geothermics, **37**, 369–399, doi: 10.1016/j.geothermics.2008.02.006.
Newman, G., and G. M. Hoversten, 2000, Solution strategies for two-and three-dimensional electromagnetic inverse problems: Inverse Problems, **16**, 1357, doi: 10.1088/0266-5611/16/5/314.
Oye, V., N. Langet, M. Hasting, I. Lecomte, M. Messeiller, and P. Reid, 2012, Microseismic monitoring of the hydraulic stimulation at the Paralana enhanced geothermal system, South Australia: First Break, **30**, 91–95, doi: 10.3997/1365-2397.30.7.60349.
Peacock, J., D. Alumbaugh, M. Mitchell, and C. Hartline, 2022, Repeat magnetotelluric measurements to monitor The Geysers steam field in Northern California: 47th workshop on Geothermal Reservoir Engineering.
Peacock, J., T. Earney, M. Mangan, W. Schermerhorn, J. Glen, M. Walters, and C. Hartline, 2020, Geophysical characterization of the Northwest Geysers geothermal field, California: Journal of Volcanology and Geothermal Research, **399**, 106882, doi: 10.1016/j.jvolgeores.2020.106882.
Peacock, J., S. Thiel, G. Heinson, and P. Reid, 2013, Time-lapse magnetotelluric monitoring of an enhanced geothermal system: Geophysics, **78**, no. 3, B121–B130, doi: 10.1190/geo2012-0275.1.
Peacock, J., S. Thiel, P. Reid, and G. Heinson, 2012, Magnetotelluric monitoring of a fluid injection: Example from an enhanced geothermal system: Geophysical Research Letters, **39**, L18403, doi: 10.1029/2012GL053080.
Sanyal, S., and S. Enedy, 2011, Fifty years of power generation at The Geysers geothermal field, California — The lessons learned: 36th Workshop on Geothermal Reservoir Engineering.
Tester, J., B. Anderson, A. Batchelor, D. Blackwell, R. DiPippo, E. Drake, and J. Garnish, 2006, The future of geothermal energy: Massachusetts Institute of Technology, 358.
Um, E., M. Commer, and G. Newman, 2014, A strategy for coupled 3D imaging of large-scale seismic and electromagnetic data sets: Application to subsalt imaging: Geophysics, **79**, no. 3, ID1–ID13, doi: 10.1190/geo2013-0053.1.
Velasco, M., D. Alumbaugh, and E. Schnetzler, 2018, Multiphysics data modeling and imaging for exploration in the southern Rocky Mountains: Interpretation, **6**, no. 3, SG59–SG78, doi: 10.1190/INT-2017-0215.1.
Wannamaker, P., V. Maris, and M. Kordy, 2017, Joint 3D inversion of ZTEM airborne and ground MT data with application to geothermal exploration: AGU Fall Meeting Abstracts.
Wannamaker, P., P. Rose, W. Doerner, B. Berard, J. McCulloch, and K. Nurse, 2004, Magnetotelluric surveying and monitoring at the Coso geothermal area, California, in support of the enhanced geothermal systems concept: Survey parameters and initial results: 29th Workshop on Geothermal Reservoir Engineering.
Wilt, M., R. Mallan, P. Kasameyer, and B. Kirkendall, 2002, 3D extended logging for geothermal resources: Field trials with the Geo-BILT system: 27th Workshop on Geothermal Reservoir Engineering, Stanford University.
Wohlenberg, J., and H. Keppler, 1987, Monitoring and interpretation of seismic observations in hot dry rock geothermal energy systems: Geothermics, **16**, 441–445, doi: 10.1016/0375-6505(87)90025-3.
Zhang, H., and C. Thurber, 2003, Double-difference tomography: The method and its application to the Hayward fault, California: Bulletin of the Seismological Society of America, **93**, 1875–1889, doi: 10.1785/0120020190.
Zhang, H., and C. Thurber, 2006, Development and applications of double-difference seismic tomography: Pure and Applied Geophysics, **163**, 373–403, doi: 10.1007/s00024-005-0021-y.
Zhu, W., and G. Beroza, 2019, PhaseNet: A deep-neural-network-based seismic arrival-time picking method: Geophysical Journal International, **216**, 1831–1841, doi: 10.1093/gji/ggy529.
Zhu, W., I. McBrearty, S. Mousavi, W. Ellsworth, and G. Beroza, 2022, Earthquake phase association using a Bayesian Gaussian mixture model: Journal of Geophysical Research: Solid Earth, **127**, e2021JB023249, doi: 10.1029/2021JB023249.

Biographies and photographs of the authors are not available.